

LINEAR AND NONLINEAR INFRASOUND PROPAGATION TO 1000 KM

Catherine de Groot-Hedlin

**Scripps Institution of Oceanography
University of California, San Diego
9500 Gilman Drive
La Jolla, CA 92093-0225**

15 December 2015

Final Report

APPROVED FOR PUBLIC RELEASE; DISTRIBUTION IS UNLIMITED.



**AIR FORCE RESEARCH LABORATORY
Space Vehicles Directorate
3550 Aberdeen Ave. SE
AIR FORCE MATERIEL COMMAND
Kirtland AFB, NM 87117**

DTIC COPY

NOTICE AND SIGNATURE PAGE

Using Government drawings, specifications, or other data included in this document for any purpose other than Government procurement does not in any way obligate the U.S. Government. The fact that the Government formulated or supplied the drawings, specifications, or other data does not license the holder or any other person or corporation; or convey any rights or permission to manufacture, use, or sell any patented invention that may relate to them.

This report was cleared for public release by the PRS OPSEC Office and is available to the general public, including foreign nationals. Copies may be obtained from the Defense Technical Information Center (DTIC) (<http://www.dtic.mil>).

AFRL-RV-PS-TR-2016-0017 HAS BEEN REVIEWED AND IS APPROVED FOR PUBLICATION IN ACCORDANCE WITH ASSIGNED DISTRIBUTION STATEMENT.

//SIGNED//

Robert Raistrick
Project Manager, AFRL/RVBYE

//SIGNED//

Glenn M. Vaughan, Colonel, USAF
Chief, Battlespace Environment Division

This report is published in the interest of scientific and technical information exchange, and its publication does not constitute the Government's approval or disapproval of its ideas or findings.

REPORT DOCUMENTATION PAGE				Form Approved OMB No. 0704-0188	
Public reporting burden for this collection of information is estimated to average 1 hour per response, including the time for reviewing instructions, searching existing data sources, gathering and maintaining the data needed, and completing and reviewing this collection of information. Send comments regarding this burden estimate or any other aspect of this collection of information, including suggestions for reducing this burden to Department of Defense, Washington Headquarters Services, Directorate for Information Operations and Reports (0704-0188), 1215 Jefferson Davis Highway, Suite 1204, Arlington, VA 22202-4302. Respondents should be aware that notwithstanding any other provision of law, no person shall be subject to any penalty for failing to comply with a collection of information if it does not display a currently valid OMB control number. PLEASE DO NOT RETURN YOUR FORM TO THE ABOVE ADDRESS.					
1. REPORT DATE (DD-MM-YYYY) 15-12-2015		2. REPORT TYPE Final Report		3. DATES COVERED (From – To) 11 Jun 2013 – 30 Sep 2015	
4. TITLE AND SUBTITLE Linear and Nonlinear Infrasound Propagation to 1000 km				5a. CONTRACT NUMBER FA9453-13-C-0280	
				5b. GRANT NUMBER	
				5c. PROGRAM ELEMENT NUMBER 62601F	
6. AUTHOR(S) Catherine de Groot-Hedlin				5d. PROJECT NUMBER 1010	
				5e. TASK NUMBER PPM00018854	
				5f. WORK UNIT NUMBER EF121974	
7. PERFORMING ORGANIZATION NAME(S) AND ADDRESS(ES) Scripps Institution of Oceanography University of California, San Diego 9500 Gilman Drive La Jolla, CA 92093-0225				8. PERFORMING ORGANIZATION REPORT NUMBER	
9. SPONSORING / MONITORING AGENCY NAME(S) AND ADDRESS(ES) Air Force Research Laboratory Space Vehicles Directorate 3550 Aberdeen Avenue SE Kirtland AFB, NM 87117-5776				10. SPONSOR/MONITOR'S ACRONYM(S) AFRL/RVBYE	
				11. SPONSOR/MONITOR'S REPORT NUMBER(S) AFRL-RV-PS-TR-2016-0017	
12. DISTRIBUTION / AVAILABILITY STATEMENT Approved for public release; distribution is unlimited. (377ABW-OPS-16-1064 dtd 19 Feb 2016)					
13. SUPPLEMENTARY NOTES					
14. ABSTRACT The Navier-Stokes equations have been solved using a finite-difference, time-domain (FDTD) approach for axi-symmetric environmental models, allowing three-dimensional acoustic propagation to be simulated using a two dimensional Cylindrical coordinate system. A method to stabilize the FDTD algorithm in a viscous medium at atmospheric densities characteristic of the lower thermosphere is described. The stabilization scheme slightly alters the governing equations, but results in quantifiable dispersion characteristics. It is shown that this method leaves sound speeds and attenuation unchanged at frequencies that are well resolved by the temporal sampling rate, but strongly attenuates higher frequencies. Numerical experiments are performed to assess the effect of source strength on the amplitudes and spectral content of signals recorded at ground level at a range of distances from the source. It is shown that the source amplitudes have a stronger effect on a signal's dominant frequency than on its amplitude. Applying the stabilized code to infrasound propagation through realistic atmospheric profiles shows that nonlinear propagation alters the spectral content of low amplitude thermospheric signals, demonstrating that nonlinear effects are significant for all detectable thermospheric returns.					
15. SUBJECT TERMS Infrasound, nonlinear propagation					
16. SECURITY CLASSIFICATION OF:			17. LIMITATION OF ABSTRACT	18. NUMBER OF PAGES	19a. NAME OF RESPONSIBLE PERSON
a. REPORT	b. ABSTRACT	c. THIS PAGE			Robert Raistrick
Unclassified	Unclassified	Unclassified	Unlimited	38	19b. TELEPHONE NUMBER (include area code)

This page is intentionally left blank.

Table of Contents

1. Summary	1
2. Introduction.....	1
3. Technical Approach	3
3.1. Governing Equations for Infrasound Propagation	3
A. Linear propagation	6
B. Nonlinear propagation in an inviscid medium	6
C. Nonlinear propagation in a viscous medium.....	7
3.2. The FDTD Numerical Algorithm	7
A. The FDTD grids	7
B. Numerical stability and dispersion relations	10
C. Source fields	14
D. Computation windows	14
4. Results and Discussion	15
A. Model 1: A Uniform Halfspace	16
B. Model 2: A Bilinear Halfspace.....	19
C. Model 3: Propagation through the stratosphere and thermosphere.....	22
5. Conclusions.....	25
References.....	27
List of Symbols, Abbreviations, and Acronyms	30

Figures

1. The FDTD model grid setup -----	8
2. Profiles of a) density, b) sound speed, and c) attenuation as a function of altitude --	13
3. FDTD Pressure fluctuation snapshots, with superimposed ray solutions -----	15
4. Pressure waveforms for nonlinear propagation in a uniform halfspace -----	17
5. Spectra for waveforms in a uniform halfspace with varying source amplitudes ----	18
6. Variation in waveform amplitude and peak frequency in a uniform halfspace -----	19
7. a) sound speed profile for a bilinear halfspace b) Ray solution with superimposed FDTD pressure solution -----	20
8. Spectra for waveforms in a bilinear halfspace with varying source amplitudes ----	21
9. Variation in waveform amplitude and peak frequency in a bilinear halfspace -----	21
10. Waveforms computed by FDTD, with predicted ray arrival times-----	23
11. Spectra for waveforms in a realistic atmospheric model -----	24
12. Peak frequencies and TL as a function of range for a realistic atmosphere-----	25

1. SUMMARY

The purpose of this project was to develop both linear and nonlinear numerical modeling codes for infrasound propagation and to use them to compute propagation through realistic atmospheric models. The objective was to determine whether nonlinear effects have a bearing on estimates of source magnitudes derived using either infrasound amplitudes or dominant frequencies. Nonlinearity is expected to primarily affect the near-source regions for large explosions or naturally occurring events, and infrasound propagation in the thermosphere, where ambient pressures are extremely low. Other areas in which nonlinearity may play a role is in the infilling of acoustic shadow zones, and propagation near caustics.

The Navier-Stokes equations are solved using a finite-difference, time-domain (FDTD) approach for axi-symmetric environmental models, allowing three-dimensional acoustic propagation to be simulated using a two dimensional Cylindrical coordinate system. A method to stabilize the FDTD algorithm in a viscous medium at atmospheric densities characteristic of the lower thermosphere is described. The stabilization scheme slightly alters the governing equations, but results in quantifiable dispersion characteristics. It is shown that this method leaves sound speeds and attenuation unchanged at frequencies that are well resolved by the temporal sampling rate, but strongly attenuates higher frequencies. Numerical experiments are performed to assess the effect of source strength on the amplitudes and spectral content of signals recorded at ground level at a range of distances from the source. It is shown that the source amplitudes have a stronger effect on a signal's dominant frequency than on its amplitude. Applying the stabilized code to infrasound propagation through realistic atmospheric profiles shows that nonlinear propagation alters the spectral content of low amplitude thermospheric signals, demonstrating that nonlinear effects are significant for all detectable thermospheric returns.

2. INTRODUCTION

One of the primary drivers of infrasound research in the past two decades has been its application to nuclear monitoring (Brachet et.al., 2009). A key goal of this research has been to find a reliable method to estimate the source yield of large explosions based on infrasound recordings. Empirical source yield relations have been derived for the dominant period of an infrasound signal (Revelle, 1997; Ens, 2012) and for its amplitude (Blanc et.al, 1997; ANSI, 1983) based on observations of a large number of nuclear explosions or bolides. Large variations in the yield estimates remain because these relations do not take into account sound and wind speed variability, which strongly affects infrasound propagation (e.g. de Groot-Hedlin et.al., 2010). Le Pichon et.al. (2012) used linear parabolic equation (PE) methods to provide more realistic expressions for infrasound transmission loss (TL) for a wide range of realistic atmospheric sound speed profiles. These expressions provide an improved description of the physics of long-range propagation and are valid for both stratospheric and thermospheric ducting.

A better description of infrasound propagation, especially for large explosive sources, requires incorporating nonlinear effects into numerical modeling algorithms. Nonlinear propagation implies that the amplitude of the pressure and density perturbations due to the passage of a sound wave is a non-negligible fraction of the ambient fields. Nonlinearity affects both the amplitude and frequency of infrasound signals and therefore impacts source yield estimates. Since nonlinear effects are dependent on the absolute amplitude of acoustic arrivals, and because acoustic amplitudes decrease much more slowly for a line source than for a spherical source, numerical algorithms that compute propagation from a spherical source must be used to compare linear vs. nonlinear infrasound propagation. The finite difference time domain (FDTD) method developed here is similar to that of de Groot-Hedlin (2012) in that the sources and models are required to be axisymmetric. This requirement allows for the efficient solution of the governing equations in a 2D cylindrical coordinate system, with quantities that may vary in both the radial and vertical directions. This leads to a FDTD code that can be used to simulate 3D infrasound propagation from a spherical source.

In this paper, both linear and nonlinear FDTD propagation modeling codes are applied to several environmental models to find where nonlinearity affects the synthesized wavefields. Nonlinearity affects infrasound not only near the shock front, which is not examined here, but also affects infrasound propagation within the thermosphere, where ambient pressures are extremely low. Other areas in which nonlinearity may play a role is in the infilling of acoustic shadow zones, and propagation near caustics. Ultimately, the goal is to determine whether nonlinear effects have a bearing on estimates of source magnitudes derived using either infrasound amplitudes or dominant frequencies. However, a straight-forward application of the FDTD governing equations can be unstable in the presence of shock fronts or in viscous media at densities characteristic of the thermosphere.

Several approaches have been developed to stabilize FDTD algorithms in the presence of discontinuities. Walkington and Eversman (1986) introduced an artificial viscosity term to dissipate oscillations that are poorly resolved by the spatial grid, resulting in a dissipation term that varies with the fourth power of the frequency, in addition to the real viscous attenuation term that varies with the square of the frequency. Sparrow and Raspet (1991) use this technique to stabilize simulations of finite amplitude acoustic propagation. Marsden et.al. (2014) employ a shock-capturing filter technique that suppresses Gibbs' oscillations that arise near shock waves. It operates by applying a nonlinear low pass filter at each time step (Bogey et.al., 2009). Shepherd et.al. (2009) use the weighted essentially non-oscillatory (WENO) method to stably propagate acoustic shocks. The WENO scheme is another shock-capturing method that uses adaptive stencils to avoid interpolation across discontinuities (Shu, 1998) to avoid introducing oscillations into the solution. However, it can have the unintended effect of excessively damping relevant small-scale structure (Bogey et.al, 2009). Moreover, the WENO method is very computationally intensive as several stencils are computed at each iteration. Costa and Don (2007) employ a hybrid approach that uses the WENO scheme near discontinuities, and a central finite difference method, coupled with high order filtering, that strongly dissipates high frequency oscillations over the remainder of the grid.

Most FDTD stabilization method work by adding steps to the basic differencing schemes and in the process they alter the governing equations being modeled. This has the desired effect of attenuating high frequency fluctuations that are poorly resolved by the spatial grid but also alters the propagation velocity, although this side effect is not generally recognized. These changes result from the fact that modifying the governing equations alters the wavenumber, which is related to both the attenuation and sound speed. In many stabilization schemes, the changes to the wavenumbers are not easily quantifiable. In this report, a new method to improve the stability of the FDTD algorithm is presented. Aside from being significantly less computationally intensive than other stabilization methods, an advantage is that the frequency dependent effect on the sound speed profile and attenuation can be quantified.

This report is organized as follows. The sets of equations governing both linear and nonlinear acoustic wave propagation are derived in the Sec 3.1. In section 3.2, a robust FDTD approach to solving these equations is presented, along with a dispersion analysis of the effect of the stabilization terms on the governing equations. Several numerical examples are presented in Sec. 4 to show how the spectral content and amplitudes of infrasound signals are altered as they propagate away from the source, and the effect of increasing source amplitude on these characteristics. The report concludes with remarks on the implications of the results for nuclear monitoring and to furthering basic understanding of atmospheric properties within the thermosphere.

3. TECHNICAL APPROACH

3.1 Governing Equations for Infrasound Propagation

The fluid equations governing infrasound propagation are derived from the conservation of mass,

$$\frac{D\rho}{Dt} = -\rho \nabla \bullet \vec{v}, \quad (1)$$

the conservation of momentum which is described by the Navier Stokes equation for a viscous fluid,

$$\rho \frac{D\vec{v}}{Dt} = -\nabla p + \mu \nabla^2 \vec{v} + (\mu_b + \mu/3) \nabla (\nabla \bullet \vec{v}), \quad (2)$$

and the conservation of energy

$$\rho \frac{De}{Dt} = -p(\nabla \bullet \vec{v}) + \left[\tau_{rr} \frac{\partial v_r}{\partial r} + \tau_{rz} \frac{\partial v_r}{\partial z} + \tau_{zr} \frac{\partial v_z}{\partial r} + \tau_{zz} \frac{\partial v_z}{\partial z} \right], \quad (3)$$

where the internal energy is given by

$$e = \frac{p}{(\gamma - 1)\rho}. \quad (4)$$

This is an extended set of Navier-Stokes equations that relates the time rate of change of the density ρ and particle velocity \vec{v} and the internal energy e , to the total pressure, p , and the shear and bulk viscosities μ and μ_B . The relevant components of the stress tensor are given by

$$\tau_{rr} = \mu \left[2 \frac{\partial v_r}{\partial r} - \frac{2}{3} (\nabla \cdot \vec{v}) \right], \quad (5a)$$

$$\tau_{rz} = \tau_{zr} = \mu \left[\frac{\partial v_r}{\partial z} + \frac{\partial v_z}{\partial r} \right] \quad (5b)$$

$$\tau_{zz} = \mu \left[2 \frac{\partial v_z}{\partial z} - \frac{2}{3} (\nabla \cdot \vec{v}) \right] \quad (5c)$$

The advective derivative, $\frac{D}{Dt}$, is equal to $\frac{\partial}{\partial t} + \vec{v} \cdot \nabla$

In Eqn. (2), only the irrotational part of the particle velocity is relevant because the density is related to the divergence of the particle velocity, so it may be re-written as

$$\rho \frac{D\vec{v}}{Dt} = -\nabla p + \mu_t \nabla^2 \vec{v}, \quad (6)$$

where μ_t is the total viscosity $\mu_B + \mu/3$. In this study, the value for μ in air is set to $1.8 \times 10^{-5} \text{ kg m}^{-1} \text{ s}^{-1}$ (Pierce, 1981) and the bulk viscosity is set to zero. More realistically, the dynamic viscosity is a function of temperature (Sutherland and Bass, 2004); it varies by approximately a factor of two for realistic atmospheric temperatures up to 120 km. However, given uncertainties in attenuation mechanisms at high altitude (Akintunde and Petculescu, 2014), the viscosity is represented by a constant in this study.

Equations (1), (3), (4) and (6) form a complete set of governing equations for acoustic propagation in a viscous medium. Thermal conductivity and molecular relaxation are neglected; these processes have little effect at infrasound frequencies (Sutherland and Bass, 2004). The equations do not include gravity terms, so they apply to frequencies above the natural buoyancy frequency of the atmosphere (the Brunt-Vaisala frequency), which ranges from about 1 mHz in the troposphere to 3 mHz in the stratosphere and thermosphere (e.g. Lingeitch *et al* 1999). This set of equations is similar to that developed in Wochner *et. al.* (2005), Shepherd *et. al.* (2009), and de Groot-Hedlin (2012) except that the energy equation is used instead of the entropy balance equation.

Equations (1), (3) and (4) may be combined to show that the pressure and density are related as

$$\frac{Dp}{Dt} = c^2 \frac{D\rho}{Dt}, \quad (7)$$

for linear propagation in an ideal gas, where c is the local sound speed. Combining Eqs. (1) and (7) yields

$$\frac{Dp}{Dt} = -\rho c^2 \nabla \cdot \vec{v}, \quad (8)$$

Equations (6) and (8) form a complete set of governing equations for linear acoustic propagation.

In the absence of shear viscosity and other absorption effect, i.e. in an isentropic process in an ideal gas, eqns. (1), (3), and (4) may be combined to show that the pressure is related to the density as

$$\frac{p}{p_o} = \left(\frac{\rho}{\rho_o} \right)^\gamma, \quad (9)$$

where the o subscripts indicate ambient values, and γ is the specific heat ratio, which is 1.4 in air. Equations (1), (6) and (9) form a complete set of governing equations for acoustic propagation in an isentropic medium.

In what follows, the second set of equations (6 and 8) is used to derive the coupled differential equations for linear acoustic propagation, and the third set (Eqs. (1), (6) and (9)) is used to derived the equivalent expressions for nonlinear propagation for a medium without viscosity. The advantage of using the latter set of equations for the nonlinear problem is that we avoid direct computation of the perturbed sound speed. For the linear problem, perturbations in the sound speeds due to the passage of an acoustic pulse are included in second and higher order terms and are neglected. Finally, the first set of equations (1, 3, 4, and 6) is used to compute nonlinear propagation through a viscous atmosphere.

The following derivations for the equations governing both linear and nonlinear propagation make the assumption that the ambient temperature, pressure and density fields vary only with altitude. This is a realistic representation of the atmosphere to first order, as ambient density and pressure variations are due to the effects of gravity. Since the ambient densities and pressures are stratified by gravity even though gravity terms are not explicitly included in this formulation, terms involving vertical gradients of the ambient pressure and density fields are omitted. Wind is also neglected in this study in order to more accurately isolate the effects of differences in linear vs. nonlinear propagation. An axisymmetric cylindrical coordinate system is used for each formulation, leading to a code that may be used to compute infrasound propagation from a spherical source embedded in a realistic atmosphere.

A. Linear propagation:

If the ambient pressure p_o , density, ρ_o , and temperature vary only with altitude and are in hydrostatic equilibrium, then Eqs. (8) and (6) may be linearized as

$$\frac{\partial p_s}{\partial t} = -\rho_o c_o^2 \left(\frac{\partial v_r}{\partial r} + \frac{\partial v_z}{\partial z} + \frac{v_r}{r} \right), \quad (10)$$

and

$$\frac{\partial v_r}{\partial t} = -\frac{1}{\rho_o} \frac{\partial p_s}{\partial r} + \frac{\mu_t}{\rho_o} \left(\frac{\partial^2 v_r}{\partial r^2} + \frac{1}{r} \frac{\partial v_r}{\partial r} + \frac{\partial^2 v_r}{\partial z^2} - \frac{v_r}{r^2} \right), \quad (11a)$$

$$\frac{\partial v_z}{\partial t} = -\frac{1}{\rho_o} \frac{\partial p_s}{\partial z} + \frac{\mu_t}{\rho_o} \left(\frac{\partial^2 v_z}{\partial r^2} + \frac{1}{r} \frac{\partial v_z}{\partial r} + \frac{\partial^2 v_z}{\partial z^2} \right), \quad (11b)$$

where p_s denotes the perturbed pressure and the perturbed particle velocity has been written as $\vec{v} = [v_r, 0, v_z]$. This is a valid approximation as long as the perturbed quantities are a negligible fraction of the ambient quantities.

B. Nonlinear propagation in an inviscid medium:

In the nonlinear, inviscid case, perturbed quantities may be large so higher order terms are retained. In this case, Eq. (1) becomes

$$\frac{\partial \rho_s}{\partial t} = -(\rho_o + \rho_s) \left(\frac{\partial v_r}{\partial r} + \frac{v_r}{r} + \frac{\partial v_z}{\partial z} \right) - \left(v_r \frac{\partial \rho_s}{\partial r} + v_z \frac{\partial \rho_s}{\partial z} \right), \quad (12)$$

and Eq. (6) becomes

$$\frac{\partial v_r}{\partial t} = -\frac{1}{(\rho_o + \rho_s)} \frac{\partial p_s}{\partial r} - \left(v_r \frac{\partial v_r}{\partial r} + v_z \frac{\partial v_r}{\partial z} \right), \quad (13a)$$

$$\frac{\partial v_z}{\partial t} = -\frac{1}{(\rho_o + \rho_s)} \frac{\partial p_s}{\partial z} - \left(v_r \frac{\partial v_z}{\partial r} + v_z \frac{\partial v_z}{\partial z} \right), \quad (13b)$$

The equation for pressure perturbations is derived from Eq. (9) as

$$p_s = p_o \left[\left(1 + \frac{\rho_s}{\rho_o} \right)^{\gamma} - 1 \right]. \quad (14)$$

C. Nonlinear propagation in a viscous medium:

For the more general case of nonlinear propagation in a viscous medium, the momentum equations are

$$\frac{\partial v_r}{\partial t} = -\frac{1}{\rho_o + \rho_s} \left[\frac{\partial p_s}{\partial r} - \mu_t \left(\frac{\partial^2 v_r}{\partial r^2} + \frac{1}{r} \frac{\partial v_r}{\partial r} + \frac{\partial^2 v_r}{\partial z^2} - \frac{v_r}{r^2} \right) \right] - \left(v_r \frac{\partial v_r}{\partial r} + v_z \frac{\partial v_r}{\partial z} \right), \quad (15a)$$

$$\frac{\partial v_z}{\partial t} = -\frac{1}{\rho_o + \rho_s} \left[\frac{\partial p_s}{\partial z} - \mu_t \left(\frac{\partial^2 v_z}{\partial r^2} + \frac{1}{r} \frac{\partial v_z}{\partial r} + \frac{\partial^2 v_z}{\partial z^2} \right) \right] - \left(v_r \frac{\partial v_z}{\partial r} + v_z \frac{\partial v_z}{\partial z} \right), \quad (15b)$$

The equation for internal energy, Eqn. 3 is given by

$$\frac{\partial e_s}{\partial t} = -\frac{p_o + p_s}{\rho_o + \rho_s} \left(\frac{\partial v_r}{\partial r} + \frac{v_r}{r} + \frac{\partial v_z}{\partial z} \right) - \left(v_r \frac{\partial e_s}{\partial r} + v_z \frac{\partial e_s}{\partial z} \right) + A, \quad (16)$$

where the attenuation term, A, is given by

$$A = \frac{\mu_t}{\rho_o + \rho_s} \left[2 \left(\left(\frac{\partial v_r}{\partial r} \right)^2 + \left(\frac{\partial v_z}{\partial z} \right)^2 + \frac{\partial v_r}{\partial r} \frac{\partial v_z}{\partial z} \right) + \left(\frac{\partial v_r}{\partial z} \right)^2 + \left(\frac{\partial v_z}{\partial r} \right)^2 - \frac{2}{3} \left(\frac{\partial v_r}{\partial r} + \frac{\partial v_z}{\partial z} \right) \left(\frac{\partial v_r}{\partial r} + \frac{v_r}{r} + \frac{\partial v_z}{\partial z} \right) \right], \quad (17)$$

Finally, the pressure perturbation is derived from the Eqn. 4 as

$$p_s = (e_o + e_s)(\gamma - 1)(\rho_o + \rho_s) - p_o. \quad (18)$$

The conservation of mass is as given by Eq. (12). This formulation could also be used for nonlinear acoustic propagation for an inviscid medium, however the equations in section 3.1 are more computationally efficient. Similarly, the equations in this section could be linearized for use in linear propagation modeling but the formulation in 3.1 is more efficient.

3.2 The FDTD Numerical Algorithm

A. The FDTD Grids

Each set of equations in the previous section is a complete set, in a form amenable to solution by the FDTD methods. Finite difference methods yield solutions to differential equations by replacing derivatives of continuous functions by their finite difference approximations formed over sets of discrete nodes.

A spatially staggered grid, as shown in Figure 1 is used to implement the FDTD algorithms. The solution domain is divided into a grid of square cells of dimension Δ , each with a uniform density ρ_o , and static sound speed c , with the axisymmetric source placed at $r=0$ along the left boundary. Pressure variables are sampled at each cell center

and particle velocities are sampled along the cell boundaries. The primary advantage of using the spatially staggered grid is that it provides second order accurate central differences over a single node for spatial derivatives in the FDTD implementation. Higher order spatial differences could lead to equivalent accuracy with a coarser grid sampling in the smooth regions of the solution. However, this leads to a loss in accuracy where the solution changes rapidly, which can result in instability. The problem of numerical stability is discussed further in section 3.2B.

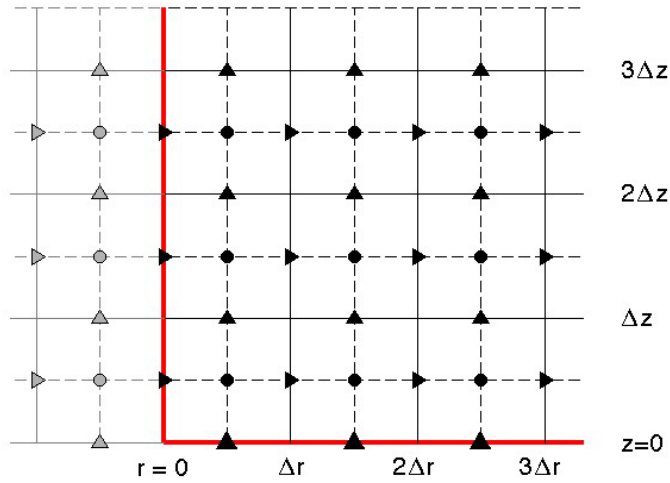


Figure 1. The FDTD model grid setup. *The spatial model is discretized as a set of cells, indicated by the solid lines, each with uniform ambient density ρ , and static sound speed c . Pressure and density perturbations are defined at nodes at each cell center, shown by circles. The horizontal particle velocity v_r (triangles pointing right) and vertical particle velocity variables v_z (triangles pointing up) nodes straddle the cell boundaries of the spatially staggered grid. The solution domain, marked by the thick line, is bounded by a rigid surface at $z=0$, and by an axis of symmetry at $r=0$. PML boundaries are used to simulate open boundaries at the top and right edges of the model.*

The spatial solution domain is bounded at the bottom by a rigid surface at $z=0$, and at left by an axis of symmetry at $r=0$. The rigid surface is specified by setting $v_z(r, z=0) = 0$. The vertical component of particle velocity v_z is anti-symmetric and other terms are symmetric about $z=0$. Since the model is axially symmetric, the radial component of particle velocity is anti-symmetric about $r=0$ and all other terms are symmetric. This means that $v_r(0, z) = 0$ at the left edge of the model, a result that can be confirmed by applying l'Hôpital's rule to Eqs. (11a). Several terms in the FDTD approximation to the governing equations require field values at $r < 0$ or $z < 0$, beyond the model boundaries.

This is resolved by making use of field symmetries. For instance, the first order spatial derivatives that appear in the attenuation terms are formed over adjacent particle velocity nodes. Thus, the $\partial \mathbf{v}_z / \partial r$ term at $r = \Delta/2$ requires values at $\mathbf{v}_z(r = -\Delta/2, z)$ and $\mathbf{v}_z(r = 3\Delta/2, z)$ to form a central difference derivative. By symmetry, $v_z(-r, z) = v_z(r, z)$ so that the $\partial \mathbf{v}_z / \partial r$ term at the leftmost nodes is computed as

$$\frac{\partial v_z(\Delta/2, z_j)}{\partial r} = \frac{v_z(3\Delta/2, z_j) - v_z(-\Delta/2, z_j)}{2\Delta} = \frac{v_z(3\Delta/2, z_j) - v_z(\Delta/2, z_j)}{2\Delta}. \quad (19)$$

Where particle velocities are required at a spatially staggered node, the particle velocities are averaged. That is, where v_z is required at a \mathbf{v}_r node as in Eq. (13a), or \mathbf{v}_r at a \mathbf{v}_z node as in Eq. (13b), the four nearest particle velocity values are averaged.

The inclusion of attenuation terms in the linear equations, and self-advection term in the nonlinear equations complicate the standard method of staggering the velocities and pressures in both space and time. These terms require that spatial and time derivatives are computed simultaneously, rather than serially as in the staggered leap-frog approach (Yee, 1966). Instead a “non-staggered leap-frog” scheme, in which centered temporal differences are formed over two time steps, is applied. This provides second order accuracy in the time derivatives and avoids the use of one-sided differences which can introduce attenuation or growth factors into the solution (de Groot-Hedlin, 2008). This approach was previously applied by Ostashev *et al* (2005) for computing acoustic waves advected through a windy atmosphere, by de Groot-Hedlin (2008) for computing acoustic propagation through a viscous atmosphere, and de Groot-Hedlin *et.al.* (2011) for computing infrasound propagation through a windy, viscous atmosphere.

The grid and time sampling rates in an FDTD simulation depend on the highest frequencies used for propagation modeling. Following Taflove and Hagness (2000), the spatial discretization used is 10 nodes per wavelength at the lowest sound speed and highest frequency of interest in the computations. For three dimensional acoustic propagation in an inviscid medium, the Courant stability limit for a Yee-type staggered leap-frog approach is given by $\Delta t \leq \Delta / (c_{\max} \sqrt{3})$. (Taflove and Hagness, 2000). In the algorithms developed here, the time derivatives are formed over two time steps so each time step is half the Courant limit. Because energy shifts from lower to higher frequencies for nonlinear computations, the requirement of 10 nodes per wavelength implies finer spatial and temporal discretizations are needed as the source amplitude increases.

A perfectly matched layer (PML) absorbing boundary condition (Berenger, 1994) that strongly absorbs outgoing waves from the computational region is imposed on the top and right side of the model. Berenger’s original PML scheme applies to a Cartesian coordinate system, but was modified for use in cylindrical coordinates by retaining the split-field formulation (the pressure in the boundary layer is split into vertically and radially propagating components) and adding cylindrical terms to the radial part of the pressure field in the boundary region. The PML method has not been modified to account for attenuation or nonlinearity.

B. Numerical stability and dispersion relations

Any solution derived using an FDTD method is inexact, in part because the continuous differential equations are replaced by discretized approximations. These errors can be quantified using dispersion relations that are derived by considering harmonic travelling wave solutions, as in Taflove and Hagness (2000) for electromagnetic problems, or de Groot-Hedlin et.al (2011) for infrasound propagation. A second reason is that the finite precision of any computer allows very small truncation errors to creep into a solution; over a very large number of time steps these errors can accumulate, causing the solution to become unstable. A third source of error is the presence of physical discontinuities in the model or shock waves in the solution. The FDTD method works by discretizing field variables over discrete stencils, or sets of nodes. An increase in the number of nodes used to approximate the derivative leads to higher orders of accuracy and allows for coarser grid discretization, so long as the function is smooth within the width of the stencil. However, the use of a wide stencil in regions where the solution undergoes rapid change - such as near shock waves or physical discontinuities in the model - seriously degrades the accuracy, and produces large oscillations in the solution. These oscillations do not decrease with increasing grid refinement and create instabilities in the FDTD method. In this section, a method is presented that suppresses instabilities that arise in regions where the kinematic viscosity is high.

A straightforward, unstabilized implementation of the FDTD method to the linear set of equations involves solving for the acoustic pressure perturbation as,

$$p^{N+1} = p^{N-1} + F_{PA}(\bar{v}^N)2\Delta t, \quad (20)$$

where the superscript represents the number of time steps, and the notation F_{PA} denotes the finite difference operator that replaces the acoustic term in Eq. (10). Equation (11) for the particle velocity can be represented as

$$\bar{v}^{N+1} = \bar{v}^{N-1} + (F_{VA}(p^N) + F_{V\mu}(\bar{v}^N))2\Delta t \quad (21)$$

where F_{VA} and $F_{V\mu}$ denote the finite difference operators for the acoustic term and the viscosity terms, respectively. Expressions for the nonlinear density and particle velocities can be represented similarly. These equations are stable for inviscid models, provided that the spatial and temporal discretizations are sufficiently fine to accurately sample the acoustic perturbations. However, the addition of the viscosity term renders these equations unstable at densities consistent with those in the thermosphere, even for linear propagation in a medium with realistic viscosities. This instability is likely due to a combination of computer truncation errors and the fact that the introduction of high kinematic viscosities can decrease the time step required to maintain stability. A full Fourier analysis that takes into account both viscosity and acoustic propagation may be required to find criterion for a stable time step. Such an analysis is beyond the scope of this paper.

Solving for the particle velocity in a two-step procedure stabilizes the equations. First, the acoustic velocity is added to provide an interim field,

$$\tilde{v} = \bar{v}^{N-1} + F_{vA}(p^N)2\Delta t \quad (22)$$

then the particle velocity is computed by applying the viscosity operator to this interim field:

$$\bar{v}^{N+1} = \tilde{v} + F_{v\mu}(\tilde{v})2\Delta t. \quad (23)$$

Combining Eqs. (22) and (23) yields a stable form for computing particle velocity:

$$\bar{v}^{N+1} = \bar{v}^{N-1} + F_{vA}(p^N)2\Delta t + F_{v\mu}(\bar{v}^{N-1} + F_{vA}(p^N)2\Delta t)2\Delta t. \quad (24)$$

This may be compared to the unstabilized form, Eq. (21). The algorithm to stabilize the nonlinear equations is similar; the acoustic and self-advection terms are first computed to find the particle velocity for the inviscid case, then the attenuation term operates on the resulting field. This method allows for the direct computation of the dispersion relation connected to the stabilized form of the FDTD equations, which leads to the effective sound speed and attenuation as a function of altitude. In what follows, a dispersion analysis is performed to demonstrate that this subtle change to the algorithm results in minimal change to solutions at frequencies that are well resolved by the grid spacing, while significantly increasing the attenuation at higher frequencies.

A simple homogeneous medium with uniform density, sound speed and viscosity is assumed. In this case the analytic solution has the form $e^{i(\vec{k}\cdot\vec{r}-\omega t)}$, so that solutions of the form

$$f_{j,m}^N = F_0 e^{i(\tilde{k}_r j\Delta + \tilde{k}_z m\Delta - \omega N\Delta t)}, \quad (25)$$

may be postulated for the pressure and particle velocities in each direction. The subscripts indicate the grid position and \tilde{k}_r and \tilde{k}_z are the finite difference approximations to the exact horizontal and vertical wavenumbers. The numerical approximation to the wavenumber differs from the analytic value of \vec{k} by an amount that depends on the spatial and temporal discretizations, the direction of propagation, as well as the frequency and sound speeds. If θ is the propagation angle with respect to the radial axis, then $\tilde{k}_r = \tilde{k} \cos \theta$ and $\tilde{k}_z = \tilde{k} \sin \theta$. For simplicity, the dispersion relation is derived here for 2D linear propagation in Cartesian coordinates, i.e. $1/r$ terms are neglected.

As in de Groot-Hedlin et.al. (2011), the following notation is adopted

$$S_t = \sin(\omega\Delta t)/\Delta t; \quad S_r = 2 \sin(\tilde{k}_r\Delta/2)/\Delta; \quad S_z = 2 \sin(\tilde{k}_z\Delta/2)/\Delta \quad (26)$$

In the limit of small Δ and Δt , these values approach ω , k_r , and k_z , respectively and $(S_r^2 + S_z^2) = \tilde{k}^2$. Using this notation, the discretized and stabilized linear equations in 2D are

$$S_t P_o = \rho_0 c^2 (S_r V_{r_o} + S_z V_{z_o}), \quad (27)$$

$$V_{r_0} S_t = \frac{S_r P_o}{\rho_o} - \frac{\mu_t}{\rho_o} (S_r^2 + S_z^2) \left(ie^{i\omega\Delta t} V_{r_0} + 2\Delta t \frac{S_r P_o}{\rho_o} \right), \quad (28)$$

and

$$V_{z_0} S_t = \frac{S_z P_o}{\rho_o} - \frac{\mu_t}{\rho_o} (S_r^2 + S_z^2) \left(ie^{i\omega\Delta t} V_{z_0} + 2\Delta t \frac{S_z P_o}{\rho_o} \right). \quad (29)$$

Equations (27) through (29) are combined to arrive at the numerical dispersion relation for the stabilized system of equations in a homogeneous, absorptive medium:

$$c^2 \frac{\mu_t 2\Delta t}{\rho_o} (S_r^2 + S_z^2)^2 - (c^2 - \frac{i\mu_t}{\rho_o} e^{i\omega\Delta t} S_t) (S_r^2 + S_z^2) + S_t^2 = 0. \quad (30)$$

For high spatial and temporal sampling rates, this equation becomes a fourth order equation for the complex-valued wavenumber \tilde{k} ,

$$c^2 \frac{\mu_t 2\Delta t}{\rho_o} \tilde{k}^4 - c^2 (1 - \frac{i\mu_t \omega}{\rho_o c^2}) \tilde{k}^2 + \omega^2 = 0 \quad (31)$$

The wavenumber is related to the frequency dependent wave speed c_p and attenuation α through $k(\omega) = \omega / c + i\alpha(\omega)$. This expression may be compared with the dispersion relation in a model with constant viscosity

$$\tilde{k}^2 = \frac{\omega^2}{c^2 (1 - i\mu_t \omega / \rho_o c^2)}, \quad (32)$$

(de Groot-Hedlin et. al, 2011), which is a second order equation for the wavenumber. Equation (32) describes the dispersion in a viscous model, which is a real, physical phenomenon that occurs in any dissipative medium. In contrast, Eq. (30) describes dispersion effects that result both from the smoothing applied in stabilizing the FDTD algorithm and from approximations that stem from discretizing the continuous governing equations. For very small time steps and low kinematic viscosities, both Eqs. (30) and (31) reduce to Eq. (32).

The frequency dependent sound speeds and attenuation were computed for a viscous medium with a realistic sound speed profile; this is the same sound speed model used in the third example in Section 4. The ambient atmospheric density profile was also computed from this profile under the assumption that the atmosphere is in hydrostatic equilibrium. Figure 2 shows the density profile, as well as the frequency dependent sound speed and attenuation profiles. The solid lines show the sound speed profiles computed using Eq. (32) for the physical dispersion. As indicated, the speed of infrasound is very weakly frequency dependent in nature, except at very low densities. As shown, sound speeds are dispersive within the thermosphere at frequencies above 5 Hz, with higher velocities at higher frequencies. The attenuation varies approximately as the square of the propagation frequency.

The dashed lines show the sound speeds and attenuations computed using Eq (31), for the stabilized FDTD equations, using a value of $\Delta t = 0.037$. This sampling rate is also used for the third example in Section 4. As shown, the 2-step stabilization procedure introduces higher attenuation values at frequencies that are poorly resolved by the sampling rate, as required, but also changes the propagation speeds. The results show that, at this sampling rate, the stabilization method does not change the physics of nonlinear propagation at frequencies at low frequencies but that at thermospheric altitudes, the dispersion that results from stabilization significantly alters sound speeds and increases attenuation at frequencies above 5 Hz.

Higher temporal sampling rates, i.e. smaller Δt , would affect the attenuation and sound speeds at higher altitudes. Thus, at least to altitudes of 120 km, the stabilization scheme causes minimal change in sound speeds and attenuation at frequencies that are well resolved by the temporal sampling rate, but higher frequencies are strongly attenuated. The attenuation shown by the dashed lines represent the minimum values at each frequency; attenuation values derived from the numerical dispersion relation, Eq. (30), are higher. The degree to which they are higher depends on the order of accuracy used for the finite difference operators. In this paper, the FDTD operators are accurate to second order.

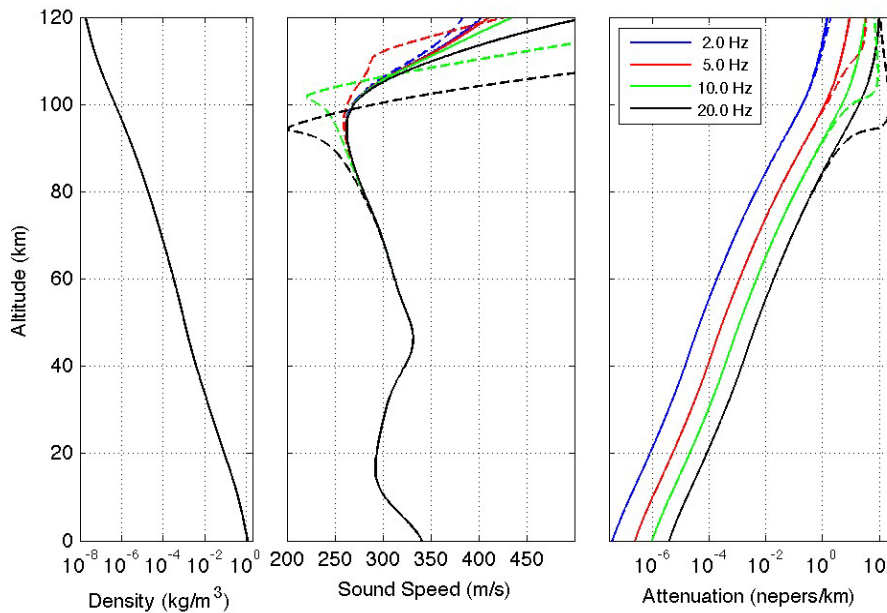


Figure 2. Profiles of a) density, b) sound speed, and c) attenuation as a function of altitude. *The solid lines show the frequency dependent sound speeds and attenuation derived from the wave equation for a viscous medium. The dashed lines show the sound speeds and attenuation values for the stabilized FDTD algorithm at a range of frequencies, computed using a value of $dt = 0.037$ s. Higher temporal sampling rates, i.e. smaller Δt , would lead to enhanced attenuation values at higher altitudes.*

C. Source Fields

For each model, the solution is initialized at $t=0$ by setting the acoustic velocities \mathbf{v}_1 and \mathbf{v}_2 to zero. For linear propagation, the pressure perturbation is initialized as

$$p_s(r,z) = \begin{cases} e^{-(R/w)^2} \cos(R\pi/8w) & R \leq 4w \\ 0 & R \geq 4w \end{cases} \quad (33)$$

where $R = \sqrt{r^2 + (z - z_o)^2}$ is the distance from the source center, located at altitude z_o and radius $r=0$, and w is the wavelength of the acoustic signal at the source altitude, at the highest frequency of interest. The source function is thus a truncated Gaussian pressure perturbation; the truncation serves to initialize the perturbations to zero outside the source region. For nonlinear propagation, the solution is initialized with a density perturbation of the form

$$\rho_s(r,z) = \begin{cases} Ae^{-(R/w)^2} \cos(R\pi/8w) & R \leq 4w \\ 0 & R \geq 4w \end{cases} \quad (34)$$

where the amplitude A controls the degree of nonlinearity. The perturbed pressure corresponding to the density perturbation is initialized using Eq. 14 prior to the time stepping loop.

D. Computation Windows

The acoustic fields computed within the FDTD method are very sparse, i.e., the pressure perturbations and particle velocity fields are zero over most of the computational domain. A method that takes advantage of this sparseness by performing computations only over non-zero field variables would significantly reduce the computational load. The approach followed here takes advantage of the fact that for long-range infrasound propagation, the field variables are non-zero over only a segment of the propagation path at any given time. This allows computations to be performed over a smaller section of the entire FDTD model domain that moves along with the pressure pulses.

An example is shown in Figure 3 for the sound speed profile shown in Figure 2, for a source at 30 km altitude. The pressure solutions, scaled by the reciprocal of the atmospheric densities, are shown at times $T=720$ s, 990 s, and 1260 s. Ray solutions are superimposed on the FDTD solutions. The vertical lines show the edges of the windows over which FDTD computations are performed at each time step. Results for this model will be examined further in section 4.

The selection of the window edges over which the computations are performed is guided in part by the ray solution for the given atmospheric model. For a given time, the right edge of the computational domain is set to a value greater than the maximum range attained by the ray solution. Similarly, the left edge is set to a value less than the minimum range attained by the ray solution. In practice, the window's right starts at a minimum of 500 nodes width and expands to the right at a velocity given by C_{right} , where C_{right} is greater than the sound speed at the source altitude. After a time delay, T_d , the left

edge of the computational regime moves at a velocity given by C_{left} , where C_{left} is less than the sound speed at the source altitude. The time delay allows for the acoustic pulse to propagate upward and out of the computational regime after a single reflection at the rigid boundary, and is given by $T_d = (z_{\text{top}} + z_o) / C_{\text{left}}$. In general, the window range is approximately equal to its total height so the reduction in computation time depends on the model geometry. For the examples shown in Section 4, the use of computation windows reduces computation time by a factor of about 4 to 5.

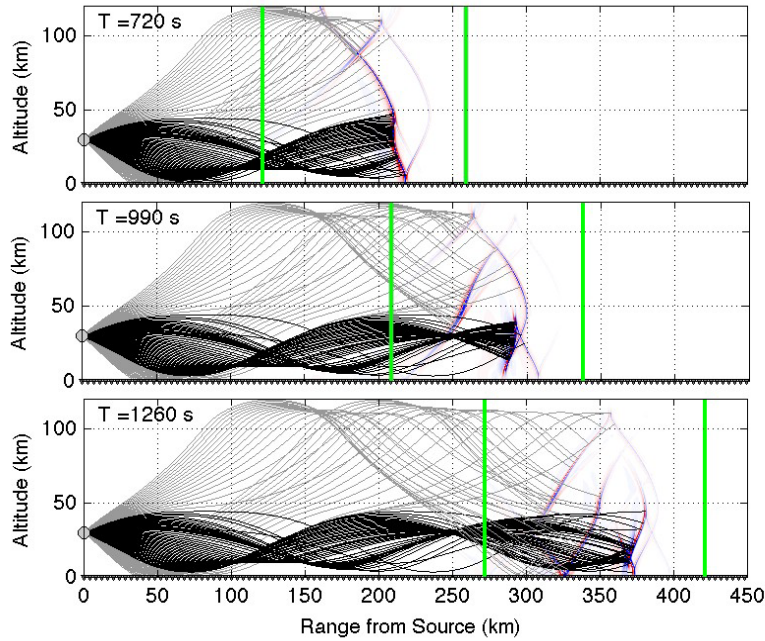


Figure 3. FDTD Pressure fluctuation snapshots, with superimposed ray solutions. *Pressure fluctuations for the sound speed profile shown in Figure 2, with a source at 30 km, for the times shown in each frame. The pressure fluctuations are scaled by the reciprocal of the square root of the atmospheric densities. Ray solutions are shown by darker lines for stratospherically ducted rays, and lighter lines for thermospherically ducted rays. The left and right edges of the FDTD computational window are shown in solid vertical lines.*

4. RESULTS AND DISCUSSION

In this section, the nonlinear FDTD infrasound propagation solver is applied to three environmental models to examine how source amplitudes affect signal strengths and peak frequencies for receivers at various distances from the source. The first two examples feature simple models with source amplitudes that range from nearly linear, with amplitudes that are a very small fraction of the ambient pressure, to strong shocks, with source pressures larger than the ambient values. In the third example, a realistic

atmospheric profile is used to investigate nonlinear effects in long-range infrasound propagation for sources that lead to weak shocks, where the acoustic pressure perturbations are less than the ambient value, but not negligible.

A. Model 1: A Uniform Halfspace

The first example involves the prediction of nonlinear acoustic signals that propagate through an inviscid uniform halfspace, terminated by a rigid surface along the bottom. The purpose of this example is to examine the changes in waveforms and spectra that result from varying the source amplitudes for the simplest possible model. The ambient density and pressure are set to their average sea level values and the ambient temperature is set to 15°C, giving a static sound speed of 340 m/s. The source is centered at an altitude of 150 m, equal to the source height used for many nuclear tests conducted as part of Operation Plumbbob at the Nevada Test site in 1957. Its shape is given by Eq. (34), where $w = 32$ m, which is equal to the wavelength at a frequency of 10.6 Hz, given the sound speed of 340 m/s. Fifty-eight virtual receivers are located at pressure nodes in the center of cells along the rigid surface, at ranges from just below the source to 5.7 km from the source, in increments of 100 m.

The numerical propagation modeling code was run for five source amplitudes with maximum density perturbations ranging from 0.1% to 80% of the ambient density; from Eq. (14) this yields pressure perturbations from .14% to 128% of the ambient pressure fields. The spatial and temporal grids for this model depend on source size, with finer discretizations for the larger amplitude sources to retain accuracy as the responses shift from lower to higher frequencies. For the smallest sources, with pressure perturbations of 0.14% and 1.4% of the ambient field, the spatial and temporal discretizations are given by $\Delta = 1.6$ m and $dt = 1.3$ ms. Given the model sound speed of 340 m/s, this spatial sampling rate gives 10 gridpoints per wavelength at a frequency of 21 Hz. For sources with maximum pressure perturbations of 29% and 61% of the ambient field, $\Delta = 1$ m and $dt = 0.84$ ms; for the largest source $\Delta = 0.8$ m and $dt = 0.67$ ms.

Figure 4 shows the infrasound responses as a function of time for virtual receivers at varying ranges, for the smallest and largest sources modeled. Figure 4a shows that the response to the low amplitude source is nearly linear, with pulses that scale as with the inverse of the distance from the source, as expected in a 3D medium (Mathews and Walker, 1970), and with shapes that do not vary with range. However, Figure 4b shows that the shape of the pressure pulses changes significantly as it propagates from a very large amplitude source; the wavefronts steepen, as is characteristic of nonlinear acoustic propagation (Pierce, 1981), and the trailing negative excursion becomes drawn out and is lower in amplitude than the positive perturbation.

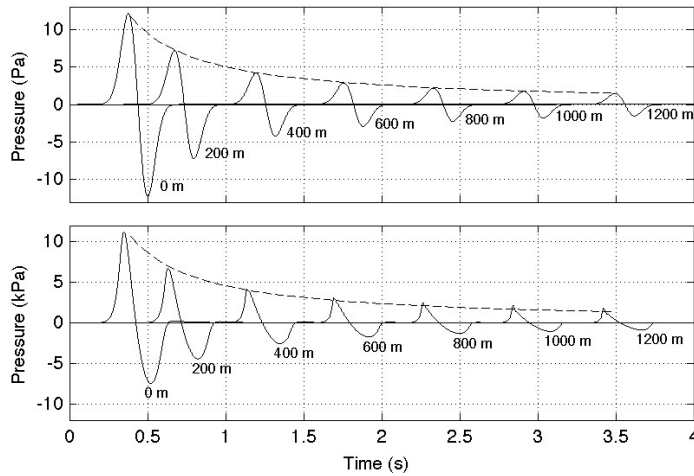


Figure 4. Pressure waveforms for nonlinear propagation in a uniform halfspace. Pressure waveforms for virtual receivers at 200 m range increments along the rigid surface, with a source at 150 m altitude for top) a small source with a maximum pressure perturbation of 0.14% of the ambient pressure and b) a large source with a maximum pressure perturbation of 128% of the ambient pressure. The dashed lines indicate the amplitude loss that would result for a linear source in a 3D medium. Note the waveform steepening as the pulse travels away from the larger source.

Changes in waveform shape are accompanied by a change in frequency content. The spectrograms in Figure 5 show how the waveform amplitude spectra evolve as a function of range from the source, for sources of varying amplitude. For the lowest source amplitude shown, the spectrum of the pulse is approximately Gaussian in shape with a single peak frequency at 2.6 Hz, and the frequency content does not vary with increased range from the source. With increased source size, the amplitude spectrum becomes flatter overall, as energy shifts from lower to higher frequency sidelobes, and the higher amplitude sources generate signals with larger numbers of narrow sidelobes.

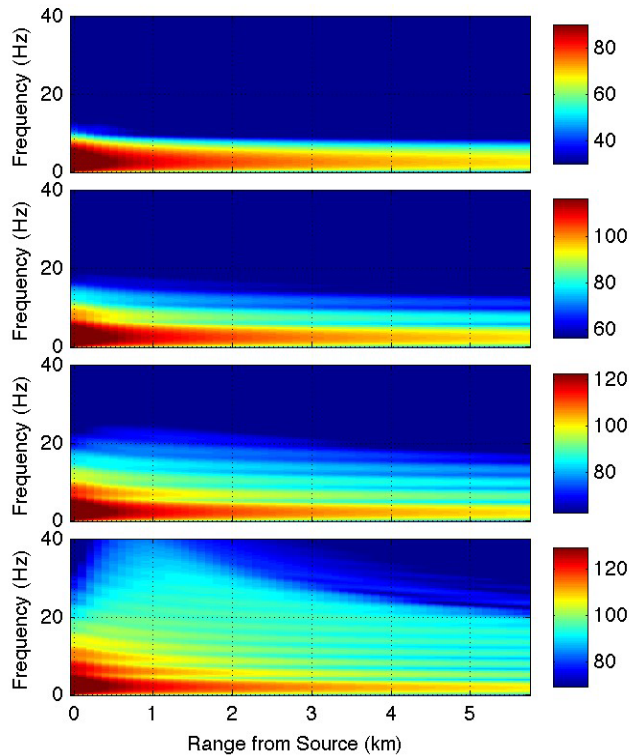


Figure 5. Spectra for waveforms in a uniform halfspace with varying source amplitudes. *Amplitude spectra for pressure waveforms propagated through an inviscid halfspace, showing the spectral variation with range for sources of increasing amplitude. From top to bottom, the ratio of the maximum pressure perturbations to the ambient pressure for each source was a) 0.01, b) 0.29, c) 0.61 and d) 1.28. The source pressures of b), c), and d) are 29.2 db, 35.7 db, and 42.1 db greater than for a). The colorbars are shifted accordingly.*

As energy is redistributed between frequencies during nonlinear propagation from the source, the dominant frequency shifts to lower values. Figure 6 shows the dominant frequency and transmission loss (TL) as a function of range for the four sources examined in Figure 5. Figure 6a shows that there is no change in the dominant frequency for the lowest source amplitude modeled, but as the source pressures increase, the shift to lower peak frequencies becomes more pronounced. Figure 6b indicates that, at all source sizes, the amplitude varies with the inverse of the distance. These results show that nonlinearity has a greater effect on the waveform spectra than on amplitudes in an inviscid halfspace model. Once the pulse pressure amplitudes have dropped to the linear regime, the form of the frequency spectrum remains unchanged as the pulse propagates further. That is, the spectra retain a series of sidelobes that are characteristic of their nonlinear origins. This is in agreement with the results of Castor et al. (2004), who found that the spectra of hydroacoustic waves also retain the nonlinear signature of a high amplitude source even after propagating great distances.

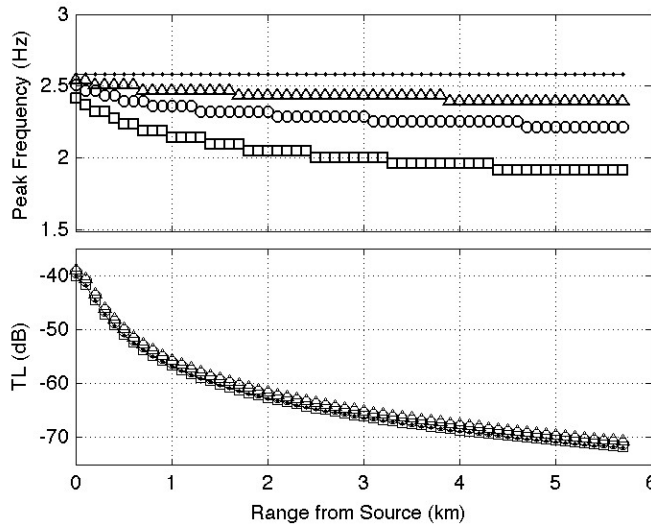


Figure 6. Variation in waveform amplitude and peak frequency in a uniform halfspace. Top) The peak frequency as a function of range for the four sources examined in Figure 5. The small dots show the dominant frequency for the smallest source amplitude. Results for the larger sources are shown, by increasing source amplitude, by triangles, circles, and squares, respectively. bottom) The transmission loss (TL) as a function of range for each source amplitude.

B. Model 2: A Bilinear Halfspace

The second example examines nonlinear infrasound propagation into a shadow zone for a model with a bilinear sound speed profile, which has a sound speed profile given by $c(z) = c(0) / \sqrt{1 + 2z/R}$, where R is the radius of curvature of a ray at the source altitude. An asymptotic solution for pressure exists for this type of sound speed profile (Pierce, 1981), which predicts the existence of a creeping wave along the surface within the shadow zone. This creeping wave has an attenuation term that is proportional to the third root of the frequency.

The sound speed profile for this model is given by $c(z) = 340 \text{ m/s} \times \sqrt{1 + z/39000}$, which gives a nearly linear sound speed decrease of 4.2 m/s per kilometer altitude. This is similar to the rate of decrease resulting from the environmental lapse rate of $6.5^\circ \text{ C per km}$, the rate of temperature decrease with altitude in a stationary atmosphere from sea level to 11 km. The source is identical to that of the previous model, and the ambient densities and pressures are set to their sea level values. The nonlinear code was run for four source amplitudes with maximum density perturbations ranging from 1% to 80% of the ambient density, equivalent to maximum pressure perturbations from 1.4% to 128% of the ambient pressure fields. Again, viscosity is neglected as it is negligible for the densities and frequencies considered here.

Figure 7 shows the sound speed profile and ray solution for this model, along with the

pressure field computed for the smallest source at time 60 s after the shot. The ray solution shows a shadow zone starting at a range of approximately 5 km from the source, but the FDTD solution indicates that acoustic energy penetrates well into the shadow zone. The nonlinear FDTD solution was run with 80 receivers along the rigid surface at intervals of 250 m, beginning just below the source.

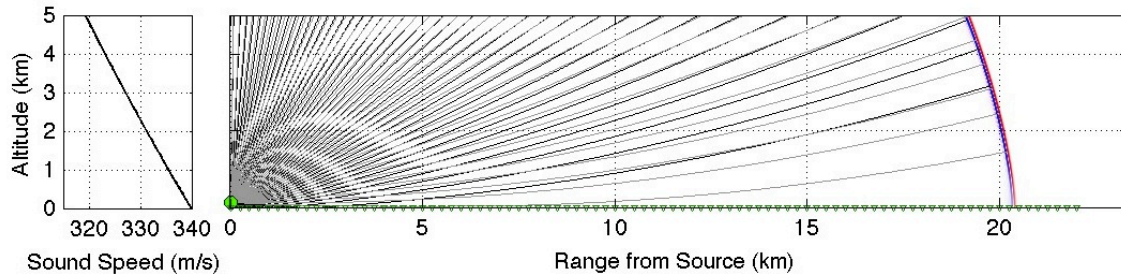


Figure 7. a) sound speed profile for a bilinear halfspace. b) Ray solution with superimposed FDTD pressure solution. *The bilinear sound speed profile used for Example 2 is shown at left and the ray solution is at right, superimposed on the FDTD solution computed at 60 seconds. The circle at 150 m altitude at left shows the source location. Triangles mark the locations of the virtual receivers. The ray solution indicates a shadow zone beyond approximately 7 km from the source, but the FDTD solution indicates that infrasound penetrates into this region.*

The spectrograms in Figure 8 show the evolution of the amplitude spectra with increasing range for this sound speed profile for sources of varying size. Compare this to Figure 5, which shows equivalent results for a halfspace model. As for the halfspace, the spectra become progressively more scalloped as the source amplitude increases, with a shift to higher frequency sidelobes. Figure 8 shows that the higher frequencies are more severely attenuated within the shadow zone than low frequencies, in agreement with the asymptotic solution for a bilinear model.

Figure 9 shows the dominant frequency and TL as a function of range for these sources. The dominant frequency shifts to lower values for propagation into a shadow zone at all the source amplitudes, as indicated in Figure 9a. In this case, the peak frequencies continue to decrease with range even after the pressure fluctuations have decreased to the linear regime, as may be expected for propagation of a creeping wave within a shadow zone. Figure 9b shows that the source amplitude does not have a significant effect on the TL, even within the shadow zone. However, the sound speed profile has a strong effect on the TL at all source amplitudes, with greater losses in signal strength within the shadow zone than for a uniform halfspace with an identical source.

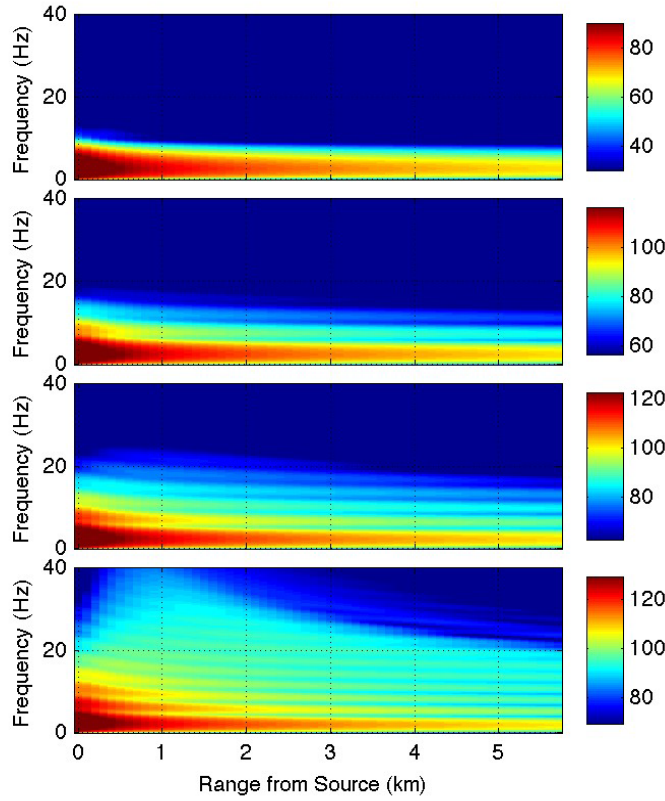


Figure 8. Spectra for waveforms in a bilinear halfspace with varying source amplitudes. As for Figure 5, but for a model with the sound speed profile shown in Figure 7.

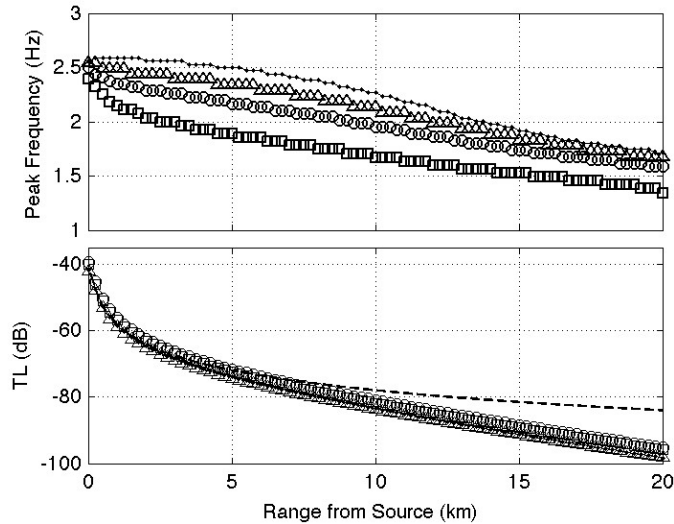


Figure 9. Variation in waveform amplitude and peak frequency in a bilinear halfspace. As for Figure 6, but for a model with the sound speed profile shown in Figure 7. The dashed line in the lower panel indicates the TL expected for a uniform halfspace.

C. Model 3: Propagation through the stratosphere and thermosphere

In the final example, infrasound propagation is computed for a viscous medium with a realistic static sound speed profile, to examine the effects of nonlinearity on propagation within the thermosphere, where the ambient density is very low, or at caustics within stratospheric ducts. Both the linear and nonlinear codes are applied to this model. The sound speed and density profiles used for this model are shown in Figure 2. Virtual infrasound receivers were placed near the rigid surface at intervals of 4 km to a range of 452 km.

The source altitude was set to 30 km, approximately the height of the Chelyabinsk bolide (de Groot-Hedlin and Hedlin, 2014) and also that of some shots used for a high-altitude infrasound calibration experiment (Herrin et.al, 2008). The source shape is given by Eq. (34) with $w = 606$ m. For the nonlinear sources, the maximum density perturbations are set to 1% and 4% of the maximum density perturbations at the source altitude, equal to 1.4% and 5.6% of the ambient pressure fields at 30 km. Although these sources have much lower amplitude than in the previous examples, the total spatial volume is about 6800 times greater, leading to a much lower peak frequency. The discretization levels were set to $\Delta = 52$ m and $dt = 0.037$ s for linear propagation modeling, and to $\Delta = 26$ m and $dt = 0.018$ s for both nonlinear propagation tests.

Akintunde and Petculescu, (2014) suggest that it may be inaccurate to treat the upper altitude as a continuum fluid at high frequencies; their results suggests the use of the Navier-Stokes equation to describe infrasound propagation may be inaccurate at altitudes above 120 km. and frequencies above 1 Hz. Accordingly, the model's maximum altitude was set to 120 km. The ray solution and the FDTD pressure solutions are shown in Figure 3 at several time points. The maximum sound speed within the stratosphere is less than the sound speed ground level, so the ray solution predicts that infrasound would be trapped within a stratospheric duct and not recorded at the surface. It predicts to a shadow zone from approximately 100 km to nearly 300 km from the source, where the first thermospheric returns arrive. The ray solution also predicts the presence of caustics within the stratosphere at ranges of approximately 125 km and 250 km from the source. The FDTD solution confirms the presence of caustics within the stratosphere.

Figure 10 shows pressure responses synthesized using the nonlinear algorithm for the smaller source, scaled by the distance from the source. The ray arrival times, indicating only arrivals that reach the ground, are shown for comparison. As shown, the arrival times for the FDTD waveforms agree with the ray travel times for direct and thermospheric arrivals, however the FDTD waveforms also include low amplitude stratospheric arrivals. Comparing this to Figure 3, it can be seen that these stratospheric arrivals are strongest where the rays nearly reach the ground.

The spectrograms for the linear and nonlinear solutions are compared in Figure 11. The colorscale of the linear modeling result is arbitrary, as doubling the source size leads to waveforms with exactly twice the amplitude with no change in the waveform shape. The spectral amplitudes for the linear results were therefore uniformly shifted to agree with the results for the smaller nonlinear source near the source origin. As shown, there is little

difference in the frequency content for the direct arrivals, at ranges from 0 to just over 100 km. A presence of a single, small sidelobe in the spectrogram for the largest amplitude source indicates a weakly nonlinear response in the near-source region.

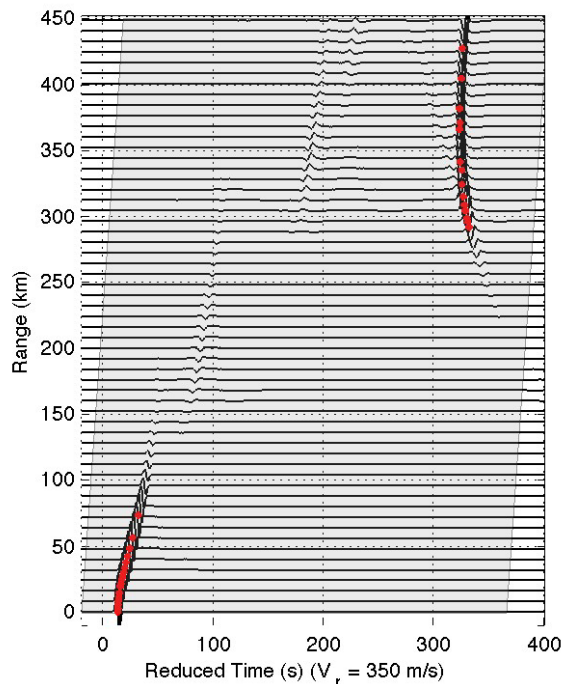


Figure 10. Waveforms computed by FDTD, with predicted ray arrival times. Waveforms synthesized by the nonlinear FDTD code, scaled by the source distance, are shown as a function of source range. The waveforms were synthesized for the sound speed and density profiles shown in Figure 2. The arrival times predicted by rays are shown by dots, showing only arrivals that reach the ground. Small amplitude stratospheric arrivals can be seen within the shadow zone predicted by the ray solution. Spectrograms in Figure 11 are computed over the time windows shown in gray.

The low frequency stratospheric arrivals within the ‘shadow zone’ between 100 and 280 km have much lower frequency content than the direct arrivals and are nearly identical for the linear and nonlinear computations. The low frequency content is characteristic of creeping waves and does not result from the shear viscosity of the medium. To verify this, the linear code was rerun for the same sound speed and density profiles, but for an inviscid medium. The results confirm that shear viscosity has no effect on the stratospheric arrivals. The similarity of the spectral results at this range indicates that the existence of caustics in the solution does not cause significant changes to the signals for relatively low amplitude sources.

Thermospheric arrivals that appear at ranges beyond 250 km have significantly lower frequency content than the direct arrivals. Comparisons between the viscous and inviscid linear solutions indicate that viscosity significantly attenuates thermospheric returns at frequencies over 0.2 Hz. Comparisons between the linear and nonlinear solutions show clear differences, more so than for the direct arrivals. For infrasound propagation

through the thermosphere, computed for finite amplitude sources, there is an opposing effect between atmospheric viscosity, which lowers the frequency of the arrivals and nonlinear effects, which steepen the wavefronts of the signals, shifting energy to higher frequency sidelobes. The spectrograms of the thermospheric arrivals show a shift of acoustic energy to higher frequency sidelobes, indicating a relatively high degree of nonlinearity even for the low amplitude source. The maximum amplitude for the thermospheric arrivals from the smaller source is about 0.1 Pa, for the larger source it is 0.5 Pa, suggesting that any detectable thermospheric returns are altered by nonlinear effects.

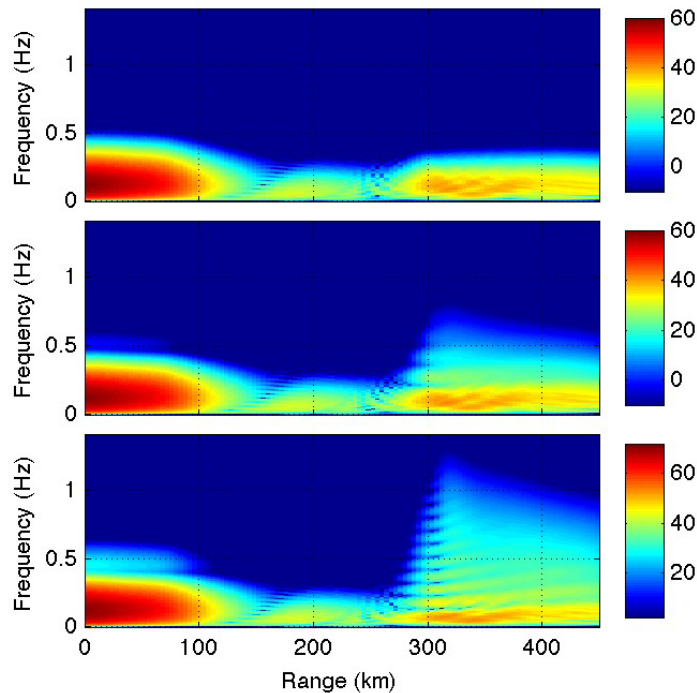


Figure 11. Spectra for waveforms in a realistic atmospheric model. *Amplitude spectra for propagation through the sound speed profile shown in Figure 3, showing the spectral variation with range for sources of increasing amplitude. The top panel presents the results for linear propagation modeling, the lower two present the results for nonlinear propagation. For the middle and bottom panels, the ratio of the maximum pressure perturbations to the ambient pressure at 30 km was middle) 0.014, bottom) 0.056. The source pressure of the larger source is 12.1 db larger than for the smaller source. The colorbar is shifted accordingly. The amplitudes for the linear results are arbitrary and were scaled to agree with the results for the smaller source near the source origin.*

Figure 12 shows the dominant frequency and TL as a function of range for this model, for the linear and nonlinear code. There are insignificant differences in the peak frequencies for the linear and nonlinear results up to 200 km range. At greater ranges, the peak frequencies for the smaller source are similar to those for the linear model; the peak

frequencies are lower for the larger source. As for the simpler models, the sound speed profile has a significant effect on the TL, but the relative source amplitude does not.

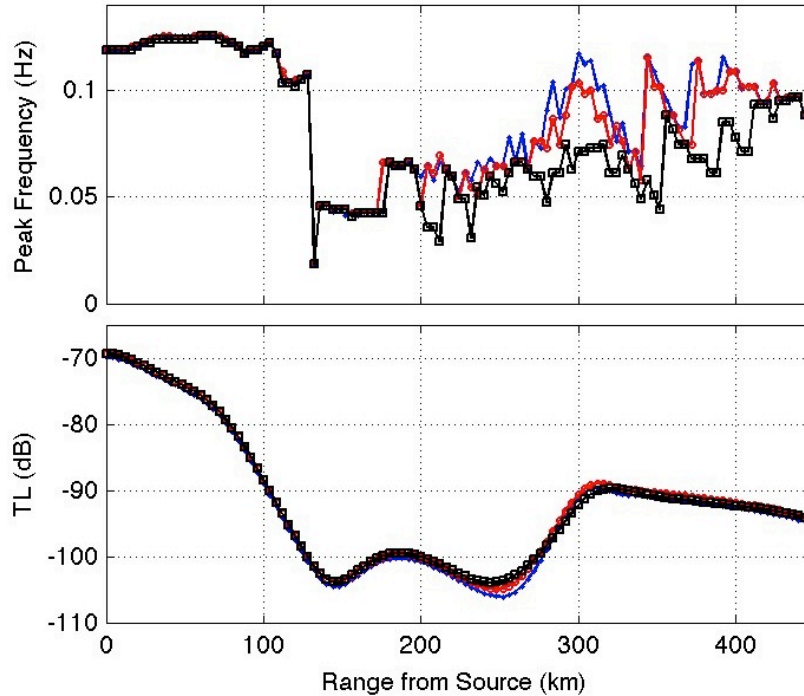


Figure 12. Peak frequencies and TL as a function of range for a realistic atmosphere. *Top) The peak frequency as a function of range for the cases examined in Figure 11. The solid line shows the dominant frequency for the linear modeling results. Results for the nonlinear sources are shown by circles for the smaller source and squares for the larger source. bottom) The transmission loss (TL) as a function of range for each source amplitude.*

5. CONCLUSIONS

FDTD algorithms to compute infrasound propagation through a viscous medium can be unstable at very low atmospheric density. A computationally efficient method to stabilize FDTD codes has been developed for both linear and nonlinear infrasound propagation modeling. The stabilization is accomplished by breaking up the computation of the particle velocities into two steps: the acoustic term is added in the first step and the viscosity operator acts upon the resulting term. This scheme results in a subtle alteration of the governing equations, and thus alters the dispersion characteristics. This dispersion is quantifiable and it is shown that sound speeds and attenuation are unchanged at frequencies that are well resolved by the temporal sampling rate, but higher frequencies are strongly attenuated, thus suppressing instability.

Applying the FDTD algorithms to strong shocks in inviscid models and weak shocks in viscous models shows that the source amplitudes have a stronger effect on the dominant frequency than on the TL. However, the amplitude and spectral content of infrasound

signals are largely controlled by the sound speed profile, indicating that the empirical source yield relations used for nuclear monitoring that are based on either the signal amplitude or peak frequency must be amended for the effective sound speed profiles. The fact that TL is not strongly dependent on source amplitude suggests that the expressions for TL developed by Le Pichon et.al. (2012) for a wide range of atmospheric conditions can be applied to propagation of weak shocks too. More work is required to examine the TL for infrasound propagation through the thermosphere for sources on the same order of magnitude as the ambient pressure.

The results from applying the stabilized FDTD code to infrasound propagation through a realistic sound speed and density profile show that thermospheric arrivals are strongly affected by nonlinear effects, more so than for arrivals near the source. Energy is shifted from lower to higher frequencies for thermospheric returns, even for signal amplitudes of less than 1 Pa. This indicates that nonlinear effects are significant for any detectable thermospheric returns.

A possible extension of this work is to apply the stabilized nonlinear FDTD code to improve our understanding of acoustic propagation in the thermosphere. Although source yield estimates can be made for infrasound returns from the thermosphere, and indeed, thermospheric returns are often the only signals observable at distance recording sites (Le Pichon et al., 2013; de Groot-Hedlin and Hedlin, 2014), infrasound propagation in the thermosphere remains poorly understood. Acoustic absorption and dispersion are poorly constrained at altitudes above 90 km (Sutherland and Bass, 2004) and the treatment of the upper atmosphere as a continuum fluid has been called into question (Akintunde and Petculescu, 2014). Comparisons between observations and the results of waveform modeling may resolve some of these unknowns.

REFERENCES

- Akintunde, A. and A. Petculescu, (2014), “Infrasonic attenuation in the upper mesosphere-lower thermosphere: A comparison between Navier-Stokes and Burnett predictions,” *J. Acoust. Soc. Am.*, **136**, pp. 1483-1486.
- American National Standards Institute, (1983), “Estimating airblast characteristics for single point explosions in air, with a guide to evaluation of atmospheric propagation and effects,” ASA S2.20-1983, (Acoustical Society of America, New York).
- Berenger, J. P., (1994), “A perfectly matched layer for the absorption of electromagnetic waves,” *J. Comput. Phys.*, **114**, pp. 1185–1200.
- Blanc, E., J.C. Millies-Lacroix, J.P. Issartel, and S. Perez, (1997), “Detection of nuclear explosions in the atmosphere,” *Chocs*, **17**, pp. 23-34.
- Bogey, C., N. De Cacqueray, and C. Bailly, (2009), “A shock-capturing methodology based on adaptive spatial filtering for high-order non-linear computations,” *J. Comput. Phys.*, **228**, pp. 1447–1465.
- Brachet, N., D. Brown, R. LeBras, P. Mialle, and J. Coyne, (2009), “Monitoring the earth’s atmosphere with the global IMS network,” In: LePichon, A., Blanc, E., Hauchecorne, A. (Eds.), *Infrasound Monitoring for Atmospheric Studies*, Springer, Dordrecht, Netherlands, pp.73–114, URL <http://www.springerlink.com/index/10.1007/978-1-4020-9508-5S>.
- Castor, K., P. Gerstoft, P. Roux, W.A.Kuperman, and B.E. McDonald, (2004), “Long-range propagation of finite-amplitude acoustic waves in an ocean waveguide,” *J. Acoust. Soc. Am.*, **116**, pp. 2004-2010.
- Costa, B. and W.S. Don, (2007), “High order hybrid central – WENO finite difference scheme for conservation laws,” *J. Comp. and Applied Math.*, **204**, pp. 209-218.
- de Groot-Hedlin, C. D., (2008), “Finite-difference time-domain synthesis of infrasound propagation through an absorbing atmosphere,” *J. Acoust. Soc. Am.*, **124**, pp. 1430-1441.
- de Groot-Hedlin, C. D., M.A.H. Hedlin, and D.P. Drob, (2010), “Atmospheric variability and infrasound monitoring,” in *Infrasound Monitoring for Atmospheric Studies*, edited by A. Le Pichon, E. Blanc, and A. Hauchecorne Springer, Dordrecht, Netherlands, Chap. 15, pp. 475–507.
- de Groot-Hedlin, C., M. Hedlin, and K. Walker, (2011), “Finite difference synthesis of infrasound propagation through a windy, viscous atmosphere: Application to a bolide explosion detected by seismic networks,” *Geophys. J. Int.*, doi: 10.1111/j.1365-246X.2010.04925.x
- de Groot-Hedlin, C., (2012), “Nonlinear synthesis of infrasound propagation through an inhomogeneous, absorbing atmosphere,” *J. Acoust. Soc. Am.*, **132**, pp. 646-656.

- de Groot-Hedlin, C.D. and M.A.H. Hedlin, (2014), “Infrasound detection of the Chelyabinsk meteor at the USArray,” *Earth Planet. Sci Lett*, <http://dx.doi.org/10.1016/j.epsl.2014.01.031>.
- Ens, T.A., P.G. Brown, and E.A. Silber, (2012), “Infrasound production by bolides: A global statistical study,” *J. Atmos. Solar-Terrest. Phys.*, **80**, pp. 208–229, doi: 10.1016/j.jastp.2012.01.018.
- Herrin, E.T., H.E. Bass, B. Andre, R.L. Woodward, D.D. Drob, M.A.H. Hedlin, M.A. Garces, P.W. Golden, D.E. Norris, C.D. de Groot-Hedlin, K.T. Walker, C.A.L. Szuberla, R.W. Whitaker, and F.D. Shields, (2008), “High-altitude infrasound calibration experiments,” *Acoustics Today*, **4**, pp. 9-21.
- Le Pichon, A., L. Ceranna, and J. Vergoz, (2012), “Incorporating numerical modeling into estimates of the detection capabilities of the IMS infrasound network,” *J. Geophys. Res.*, **117**, D05121, <http://dx.doi.org/10.1029/2011JD016670>.
- Le Pichon, A., L. Ceranna, C. Pilger, P. Mialle, D. Brown, P. Herry, and N. Brachet, (2013), “The 2013 Russian fireball largest ever detected by CTBTO infrasound sensors,” *Geophys. Res. Lett.*, **40**, pp. 3732–3737, doi: 10.1002/grl.50619.
- Lingevitch, J.F., M.D. Collins, and W.L. Siegmann, (1999), “Parabolic equations for gravity and acousto-gravity waves,” *J. Acoust. Soc. Am.*, **105**, pp. 3049-3056.
- Marsden, O., C. Bogey, and C. Bailly, (2014), “A study of infrasound propagation based on high-order finite difference solutions of the Navier-Stokes equations,” *J. Acoust. Soc. Am.*, **135**, pp. 1083-1095.
- Mathews, J. and R.L. Walker, (1970), *Mathematical methods of physics*, 2nd Ed., W.A. Benjamin, Menlo Park, California.
- Ostashev, V.E., D.K. Wilson, L. Liu, D.F. Aldridge, N.P. Symons, and D. Marlin, (2005), “Equations for finite-difference, time-domain simulation of sound propagation in moving inhomogeneous media and numerical implementation,” *J. Acoust. Soc. Am.*, **117**, pp. 503-517.
- Pierce, A. D., (1981), *Acoustics: An Introduction to its Physical Principles and Applications*, Acoustical Society of America, Woodbury, NY, pp. 1-678.
- ReVelle, D.O., (1997), “Historical detection of atmospheric impacts by large bolides using acoustic-gravity-waves,” *Annals of the New York Academy of Sciences*, **822**, 284–302. URL /<http://dx.doi.org/10.1111/j.1749-6632-1997.tb48347.x>.
- Shepherd, M. R., Gee, K. L., and Wochner, M. S. (2009). “Short-range shock formation and coalescence in numerical simulation of broadband noise propagation,” *J. Acoust. Soc. Am.*, **126**, 2886–2893.
- Shu, C.W., (1998), “Advanced Numerical Approximation of Nonlinear Hyperbolic Equations, Lecture Notes in Mathematics,” **1697**, Springer, Berlin, pp. 325–432.

- Sparrow, V. W., and R. Raspet, (1991), "A numerical method for general finite amplitude propagation in two dimensions and its application to spark pulses," *J. Acoust. Soc. Am.*, **90**, pp. 2683–2691.
- Sutherland, L.C. and H.E. Bass, (2004), "Atmospheric absorption in the atmosphere up to 160 km," *J. Acoust. Soc. Am.*, **115**, pp. 1012-1032.
- Taflove, A. and S.C. Hagness, (2000), *Computational electrodynamics: the finite-difference time-domain method*, 2nd ed., Artech House, Norwood, MA.
- Walkington, N.J. and W. Eversman, (1986), "A numerical model of acoustic choking, Part II: Shocked solutions," *J. Sound Vib.*, **104**, pp. 81-107.
- Wochner, M. S., A.A. Atchley, and V.W. Sparrow, (2005), "Numerical simulation of finite amplitude wave propagation in air using a realistic atmospheric absorption model," *J. Acoust. Soc. Am.*, **118**, pp. 2891–2898.
- Yee, K.S., (1966), "Numerical solution of initial boundary value problems involving Maxwell's equations in isotropic media," *IEEE Trans. Antennas and Propagation*, **14**, pp. 302-307.

List of Symbols, Abbreviations, and Acronyms

FDTD	Finite Difference Time Domain
TL	Transmission Loss

DISTRIBUTION LIST

DTIC/OCP

8725 John J. Kingman Rd, Suite 0944

Ft Belvoir, VA 22060-6218

1 cy

AFRL/RVIL

Kirtland AFB, NM 87117-5776

2 cys

Official Record Copy

AFRL/RVBYE/Robert Raistrick

1 cy

This page is intentionally left blank.